MFogHub: Bridging Multi-Regional and Multi-Satellite Data for Global Marine Fog Detection and Forecasting

Supplementary Material

An overview of Supplementary Material for MFogHub dataset is provided below.

- Sec. 1 and Sec. 2 provide **foundational information** about the dataset, including access to the dataset and code, as well as multi-regional details in MFogHub.
- Sec. 3 and Sec. 4 show the **data preparation process**, including marine fog annotation and sample visualization.
- Sec. 5 introduces the **evaluation metrics** used for assessing model performance.
- Sec. 6 presents **more experimental results**, covering multi-regional and satellite generalization, multi-region marine fog forecasting, and the impact of different positive-to-negative sample ratios across regions.

1. Dataset and Code Access

To comply with the CVPR anonymity guidelines and address GitHub's storage limitations, we have created an anonymized GitHub repository containing representative examples from **MFogHub** along with processing and benchmark code. The complete dataset and benchmark will be made publicly available upon acceptance of the paper. The anonymized repository is accessible at: `https://anonymous.4open.science/r/MFogHub-DE63/`.

2. Multi-Regional Information in MFogHub

The detailed information of the global multi-regional areas proposed in MFogHub is presented in Table 1, spanning multiple continents and oceans, and covering several important coastal cities and ports around the world. The abbreviations of Continents or Oceans[1] are provided below. Due to the proximity of the sub-satellite points of the FY4 series and H8/9 series satellites[2], both can collaboratively monitor most regions of the Western Pacific. This collaboration allows for mutual supplementation and significantly enhances detection capabilities.

3. Annotation of Marine Fog

Before annotating the marine fog images, it is essential to identify which time periods and maritime regions contain marine fog and to determine the evolution of the entire marine fog process. Our identification primarily relies on the following aspects:

- **Expert annotations and experience**: We collaborated with meteorological experts from meteorological centers to identify and annotate typical marine fog events based on their expertise and experience.
- **Meteorological reports and reviews**: Resources, such as published Spring 2024 Marine Weather Review [10] as shown in Table 2, provide detailed information about marine fog events, including their occurrence, regions, and types, serving as valuable references for identification.
- **Meteorological observations from ships and coastal stations**: Data sources such as International comprehensive ocean-atmosphere data set (ICOADS) [7] provide key meteorological parameters, including present weather phenomena, visibility, and relative humidity, which can be analyzed using marine fog detection criteria to further refine the data.

We utilized the annotation tool from the research [2] for marine fog monitoring based on natural-color images, as exemplified in Fig. 1 (a). This tool employs the Simple Linear

Table 1. Detailed information for multi-regional areas proposed in MFogHub, including Regions designation, Abbreviation (regions abbr.), Continent and oceans, Location, Supported satellite data, and corresponding Major City/Port.

Regions	Abbr.	Continent/ Oceans	Locations: Latitude range	Locations: Longitude range	Satellites	Major City/ Port
Yellow and Bohai Seas	Y.B.	AS/PO	28.7°N-41.5°N	116.2°E-129.0°E	FY4A, FY4B, H8/9	Tianjin
China East Sea	E.S.	AS/PO	20.0°N-32.8°N	117.0°E-129.8°E	FY4A, H8/9	Shanghai
China South Sea	S.S.	AS/PO	11.2°N-24.0°N	105.0°E-117.8°E	FY4A, H8/9	Hong Kong
Mediterranean (East)	M.E.	EU/AO	37.2°N-50.0°N	27.0°E-39.8°E	MeteoSat	Athens
Mediterranean (Central)	M.C.	EU/AO	30.0°N-42.8°N	15.0°E-27.8°E	MeteoSat	Rome
Mediterranean (West)	M.W.	EU/AO	33.0°N-45.8°N	0.0°-12.8°E	MeteoSat	Barcelona
North Sea	N.S.	EU/AO	47.2°N-60.0°N	7.8°W-5.0°E	MeteoSat	Rotterdam
Namibia	Na.	AF/IO	14.0°S-26.8°S	2.0°E-16.8°E	MeteoSat	Cape Town
Agulhas Current	A.G.	AF/IO	25.2°S-38.0°S	8.0°E-20.8°E	MeteoSat	Durban
Gulf of Alaska	G.A.	NA/PO	42.2°N-55.0°N	120.0°W-132.8°W	GOES16	Anchorage
California Current	C.C.	NA/PO	32.0°N-44.8°N	119.0°W-131.8°W	GOES16	San Francisco
Baja California	B.C.	NA/PO	22.2°N-35.0°N	109.0°W-121.8°W	GOES16, GOES17	La Paz
Gulf Stream	G.S.	NA/AO	42.0°N-54.8°N	57.0°W-69.8°W	GOES16	New York
Gulf of Mexico	G.M.	NA/GO	18.0°N-30.8°N	87.2°W-100.0°W	GOES16	New Orleans
North Brazil Current	N.B.	SA/AO	18.0°S-30.8°S	37.0°W-49.8°W	GOES16	Belém

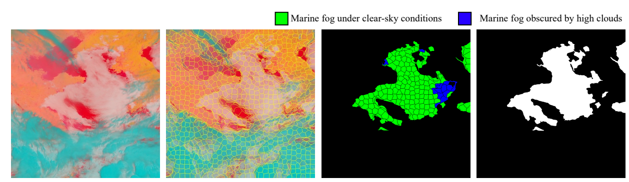

(a) False-color image **(b) Super-pixel processed** **(c) Super-pixel label** **(d) Final label**

Figure 1. The key images from the marine fog annotation process using SLIC algorithm, taking an example from Himawari-8/9 satellite data captured at 00:00 UTC on June 13, 2021.

[1]The abbreviations of Continents are: Asia (AS), Africa (AF), North America (NA), South America (SA), Antarctica (AN), Europe (EU), Australia (AU). The abbreviations of Oceans are: Pacific Ocean (PO), Atlantic Ocean (AO), Indian Ocean (IO), Southern Ocean (SO), Arctic Ocean (ArO).

[2]The FY4 series satellites have a sub-satellite point at approximately 104.7°E, while the H8/9 series satellites have a sub-satellite point at approximately 140.7°E.

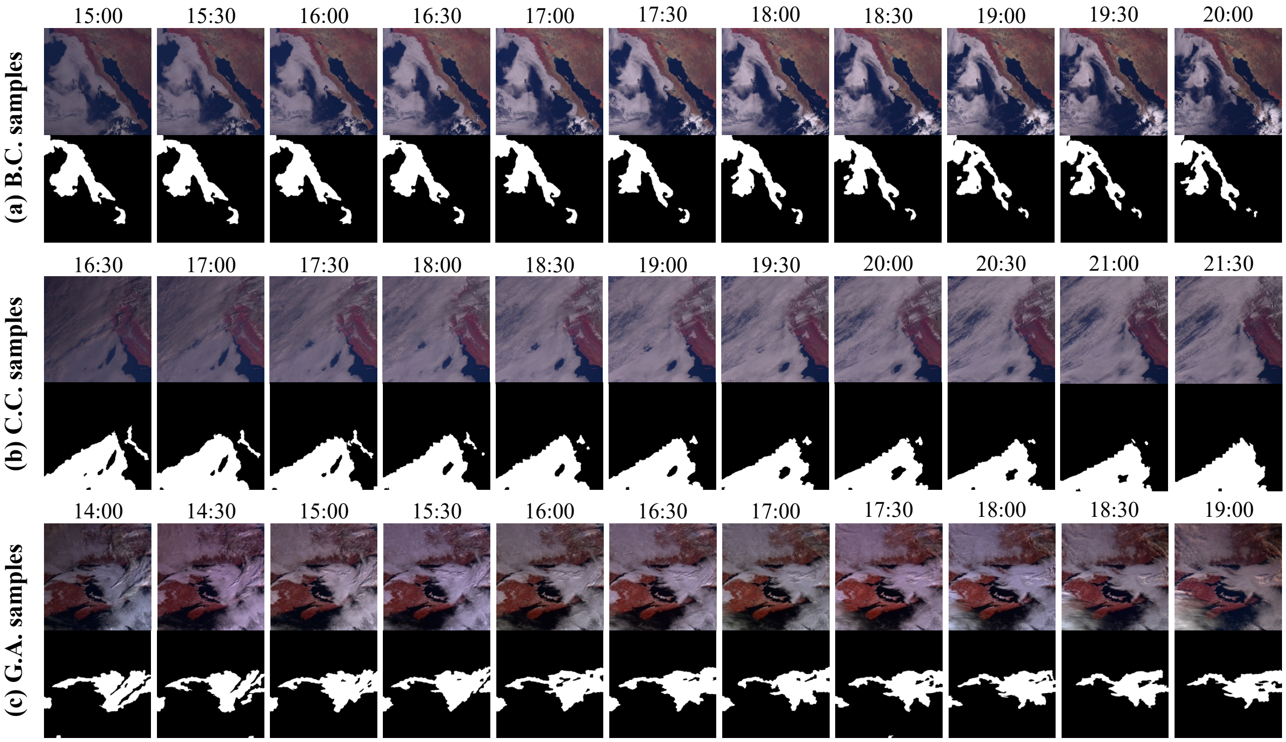

Figure 2. Visualization examples of GOES16 satellite data across three regions including true-color images and corresponding fog masks, where each row represents a distinct marine fog event. (a), (b), and (c) represent Baja California (B.C.), California Current (C.C.), and Gulf of Alaska (G.A.) region, respectively.

Table 2. Records of marine fog events from Spring 2024 Marine Weather Review [10] with detailed information, including time, intensity, minimum visibility, and regions.

	Month	Day	Intensity	Visibility	Marine fog distribution locations
1	March	22-24	Heavy Fog	$\leq$ 1km	Bohai Sea, Most of Yellow Sea, Western China East Sea
2	March	27-28	Heavy Fog	$\leq$ 1km	Central and southern Yellow Sea, North Yellow Sea
3	April	26-27	Heavy Fog	$\leq$ 1km	Most of Yellow Sea, Western China East Sea

Iterative Clustering (SLIC) algorithm [1] to achieve pixel-level annotations. Taking Himawari-8/9 data as an example, we use Band 03 (0.64μm), Band 04 (0.86μm), and Band 14 (11.20μm) to combine the natural-color image since it is feasible to highlight the features and textures of marine fog, relying on the high reflectance and low brightness temperature values of the marine fog. First, pseudo-color images are segmented into N super-pixels (set to $N = 500$ during our annotation process), as illustrated in Fig. 1 (b). For each super-pixel, three annotation options are provided: fog under clear-sky conditions, fog obscured by high clouds, and non-fog regions. These are represented in Fig. 1 (c) by green, blue, and black blocks, respectively. Since gaps may exist between super-pixels during segmentation, we further applied dilation and erosion operations to generate a complete and connected final binary mask for marine fog as shown in Fig. 1 (d).

4. MFogHub Samples

The MFogHub dataset supports multi-dimensional data retrieval, extraction, and the creation of sub-datasets tailored to specific experimental purposes. Based on the experimental design described in the main text, this section presents visualization examples of different regions under the same satellite data and of the same region under different satellite data, as illustrated in Fig. 2 - Fig. 4.

From the aspect of multi-regional, Fig. 2 provides data samples from the GOES satellite for three regions: Baja California (B.C.), California Current (C.C.), and Gulf of Alaska (G.A.). It is evident that marine fog varies significantly in terms of spatial distribution and shape across different regions. These differences are largely influenced by factors such as ocean currents and sea surface temperature variations. Additionally, during daytime fog events, imaging near dawn or dusk may be slightly affected, as seen in the first column of Fig. 2. Besides, Fig. 3 presents sequential data from the FY4A satellite for different regions, focusing on the marine fog forecasting task. The regions include the Yellow and Bohai Seas (a), the East China Sea (b), and the South China Sea (c). It can be observed that the distribution of marine fog and clouds varies significantly across regions due to differences in land-ocean configura-

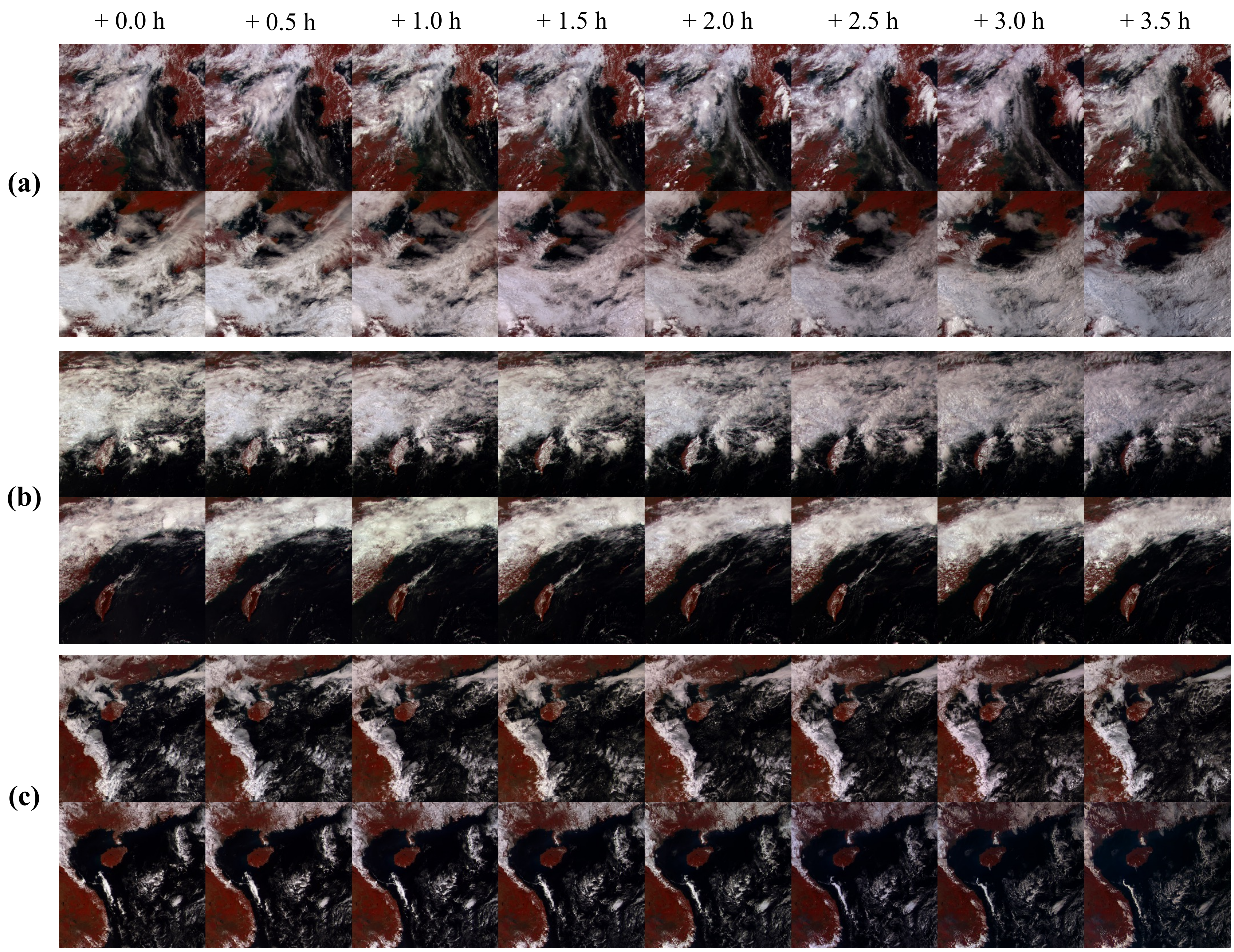

Figure 3. Visualization examples of FY4A satellite sub-dataset for the marine fog forecasting task. (a), (b), and (c) represent multiple time series samples from the Yellow and Bohai Seas, the East China Sea, and the South China Sea, respectively, with a 30-minute interval between consecutive images.

tions and cloud patterns. Over the progression of consecutive images, differences in the movement speeds of various cloud types and fog can also be seen. Notably, marine fog exhibits slower changes compared to other cloud types.

From the aspect of multi-satellite, Fig. 4 shows a comparative visualization of data collected over the Yellow and Bohai Seas from the FengYun-4A (FY4A) and Himawari-8/9 (H8/9) satellites, along with corresponding manually annotated labels, during the time period from 00:00 to 04:30 UTC on March 25, 2021. The FY4A composite image is constructed using the Band 01 (0.47μm), Band 02 (0.65μm), and Band 03 (0.825μm), while the H8 composite image is also derived from the Band 01 (0.47μm), Band 02 (0.51μm), and Band 03 (0.64μm). Notably, while the composite images generated from different spectral bands exhibit some differences, the texture patterns and the numerical distribution of values within the fog regions remain relatively consistent across the datasets. These visualizations underscore the diversity and comparability of data across regions and satellite sources, highlighting the dataset's versatility for research purposes.

5. Evaluation Metrics

We evaluate the performance of different baseline models on marine fog detection and forecasting tasks using multiple metrics in a thorough and rigorous manner.

For the marine fog detection task, as shown in the Fig. 5, a confusion matrix composed of True-Positive (TP), False-Positive (FP), False-Negative (FN) and True-Negative (TN) is derived based on the statistical results of all test samples for the marine fog category. Using this matrix, we compute several evaluation metrics, including The Critical Success Index (CSI), Recall, Precision, Accuracy and the mean Intersection over Union (mIoU) with the detailed calculation formulas provided in the Fig. 5.

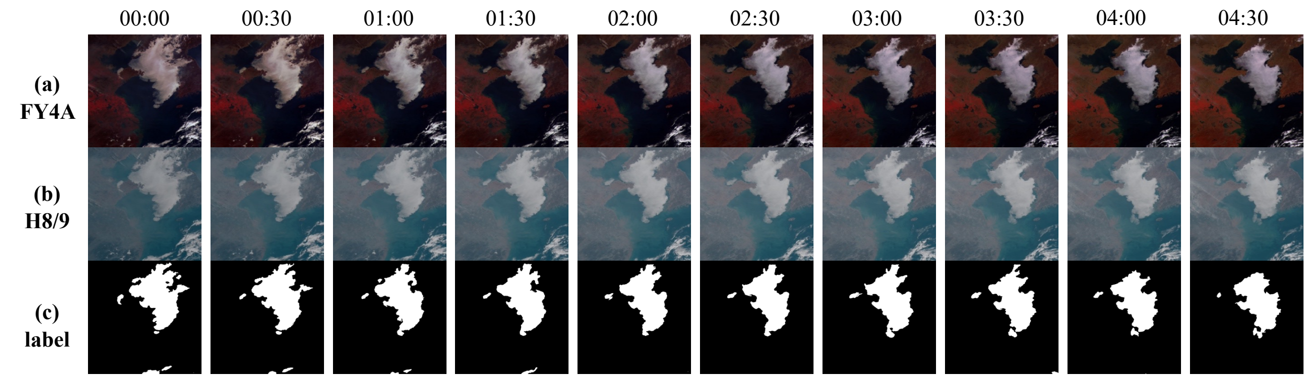

Figure 4. Visualization examples of FY4A and H8/9 satellite data with corresponding marine fog labels over the Yellow and Bohai Seas from 00:00 to 04:30 UTC on March 25, 2021.

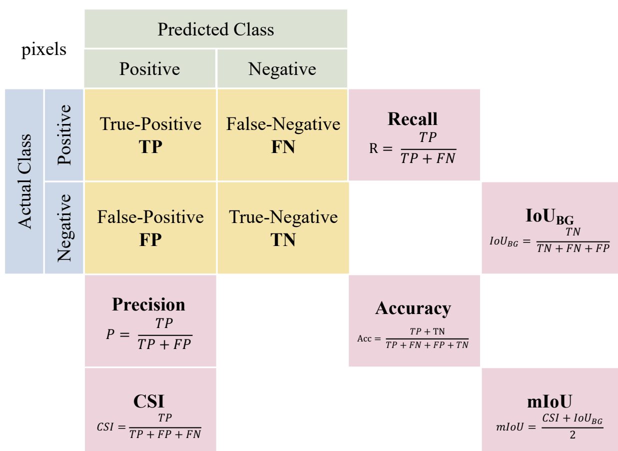

Figure 5. Confusion matrix and evaluation metrics on marine fog detection task in MFogHub on the statistical results of all test pixels.

For the marine fog forecasting task, we employ the following four evaluation metrics:

Error metrics: To measure the differences between the predicted results and the ground truth, we use the Mean Squared Error (MSE) and the Mean Absolute Error (MAE), that which can be formulated as:

$$\text{MSE} = \frac{1}{T}\sum_{t=1}^{T}\sum_{c=1}^{C}\sum_{h=1}^{H}\sum_{w=1}^{W}(y_{t,c,h,w} - \hat{y}_{t,c,h,w})^2 \tag{1}$$

$$\text{MAE} = \frac{1}{T}\sum_{t=1}^{T}\sum_{c=1}^{C}\sum_{h=1}^{H}\sum_{w=1}^{W}|y_{t,c,h,w} - \hat{y}_{t,c,h,w}| \tag{2}$$

In Equations (1) and (2), T, C, H and W represent timestamp, spectral band, height, and width of a sample, respectively; y represents the prediction, and $\hat{y}$ represents the ground truth.

Similarity metrics: To assess the similarity between the predicted results and the ground truth, we utilize the Structural Similarity Index Measure (SSIM) (Equation 3) and the Peak Signal-to-Noise Ratio (PSNR), that which can be formulated as:

$$\text{SSIM} = \frac{(2\mu_y\mu_{\hat{y}} + C_1)(2\sigma_{y\hat{y}} + C_2)}{(\mu_y^2 + \mu_{\hat{y}}^2 + C_1)(\sigma_y^2 + \sigma_{\hat{y}}^2 + C_2)} \tag{3}$$

$$\text{PSNR} = 10 \cdot \log_{10}\left(\frac{\text{MAX}^2}{\text{MSE}}\right) \tag{4}$$

In Equation (3), μ_y and $\mu_{\hat{y}}$ are the mean values of y and $\hat{y}$, σ_y^2 and $\sigma_{\hat{y}}^2$ are the variances of y and $\hat{y}$, $\sigma_{y\hat{y}}$ is the covariance of y and $\hat{y}$. C_1 and C_2 are small constants used to stabilize the division. In Equation (4), MAX is the maximum pixel value of the prediction y, and MSE is the Mean Squared Error between y and $\hat{y}$.

6. More Experimental Results

6.1. Qualitative results for satellite generalization

We provide qualitative results for the assessment of satellite generalization experiment to further validate the dataset's capability in multi-satellite evaluation and highlight the differences between various satellites. From Fig. 6 (a), it can be observed that, across different methods tested on FY4A and H8/9 datasets, H8/9 data exhibits stronger fog detection performance. However, the ability of the methods to detect smaller fog regions still requires improvement. In Fig. 6 (b), it is evident that Dlink-ViT [12] demonstrates stability in its performance across consecutive timestamps of marine fog events, with consistently accurate and continuous predictions. These visualized differences further underscore the dataset's robustness for validation purposes and its sensitivity to variations in data from different satellites, providing valuable insights for model development and evaluation.

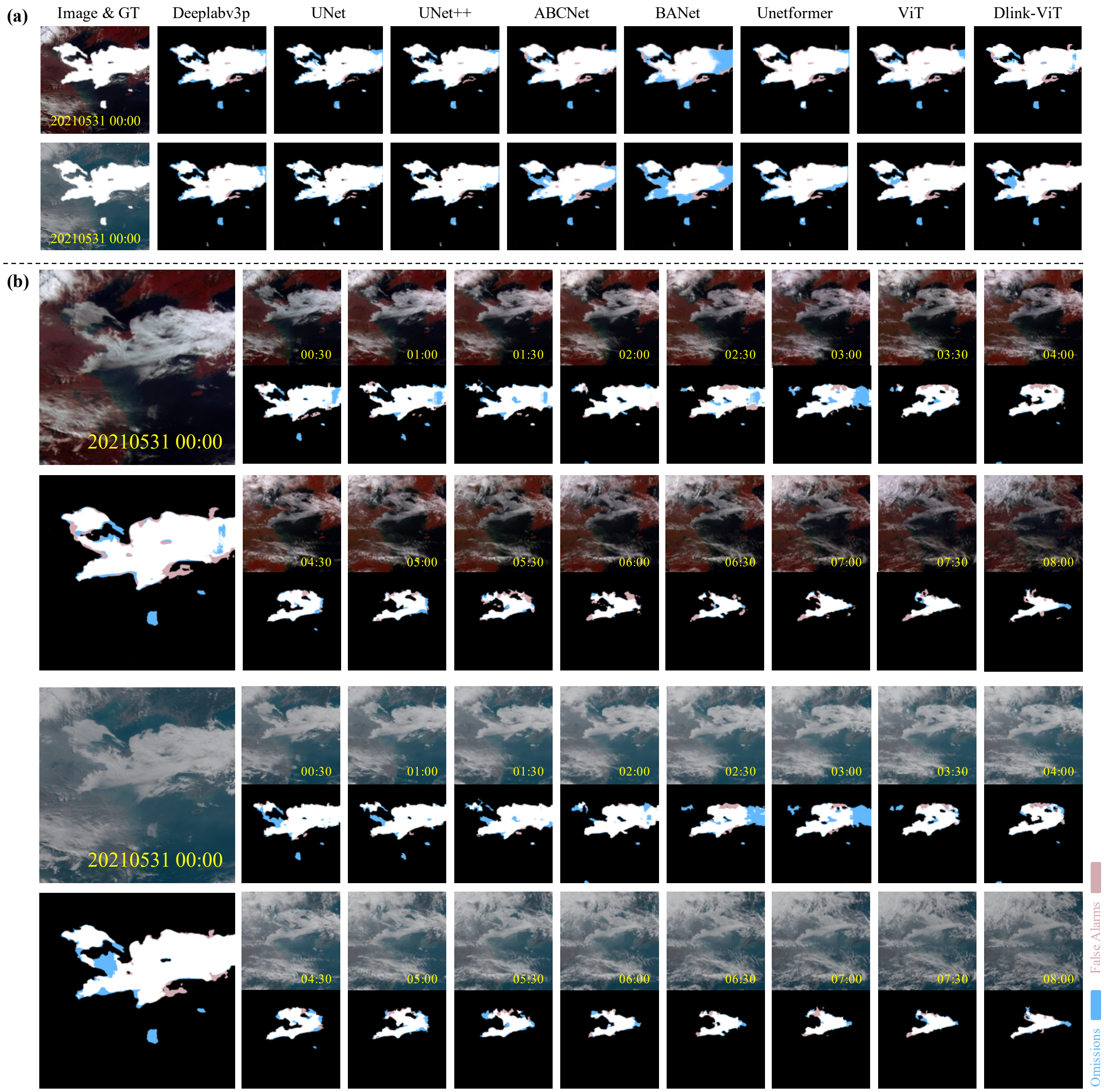

Figure 6. Qualitative visualizations of the marine fog detection task using the FY4A and H8/9 sub-datasets from MFogHub on May 31, 2021, over the Yellow and Bohai Seas. The white, blue, and red regions represent True Positives (TP), False Negatives (FN, omissions), and False Positives (FP, false alarms), respectively. (a) Comparisons of eight baseline models. (b) An illustrative example of continuous marine fog monitoring using Dlink-ViT. [12].

6.2. Qualitative results for regional generalization

We provide qualitative results as shwon in Fig. 7 for the assessment of regional generalization experiment to further validate the dataset's capability using eight baseline methods, taking the North Sea (N.S.), Mediterranean (Central) (W.C.), and Agulhas Current (A.G.) sub-dataset from MeteoSat data as an example. It highlights the differences in predictive performance across models, both spatially (across regions) and temporally (over time steps). It underscores the importance of qualitative analysis as a complement to quantitative metrics, particularly for capturing subtle variations in model performance. Furthermore, the mod-

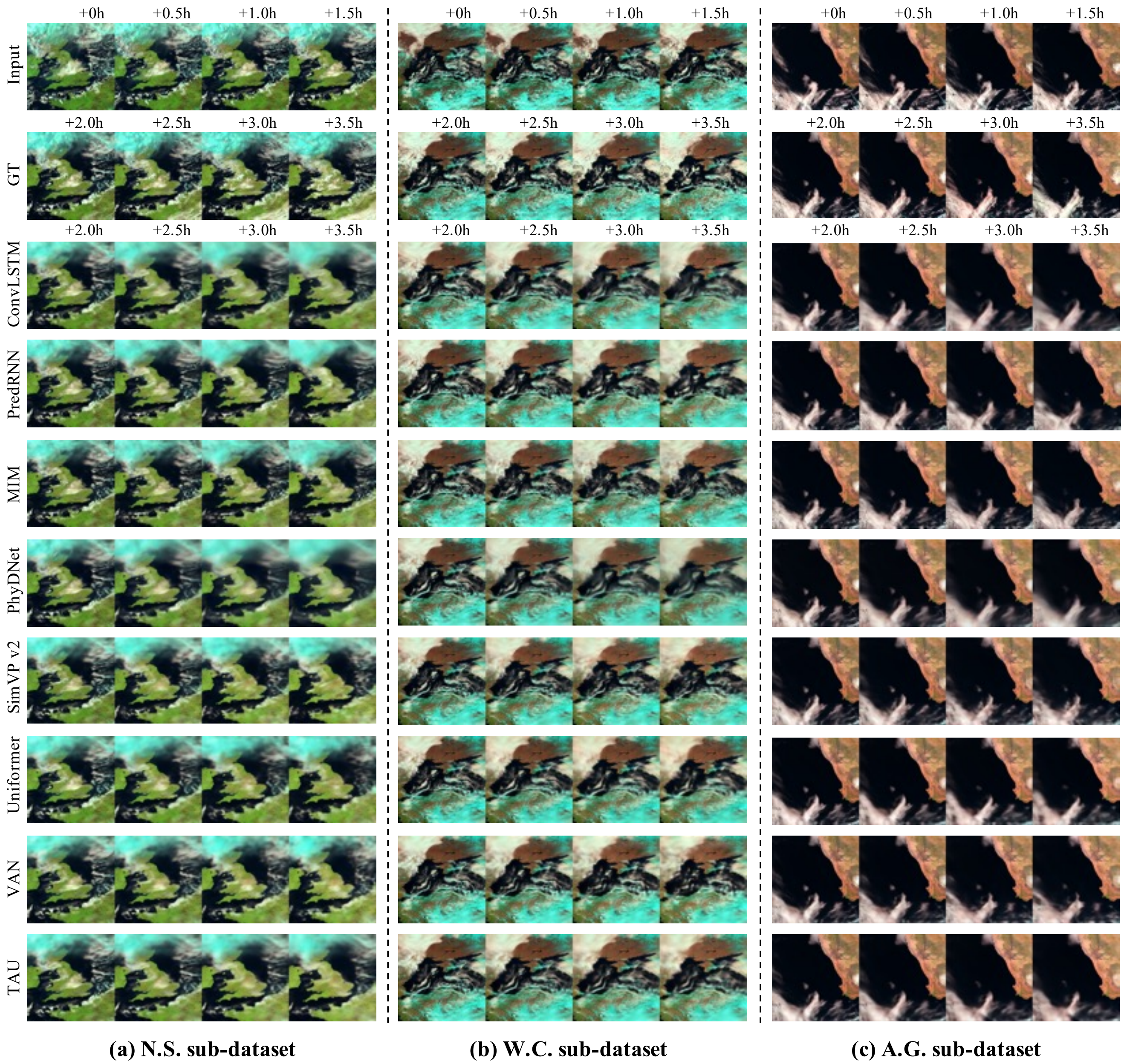

Figure 7. Qualitative visualizations of the marine fog forecasting results across different baseline methods on the North Sea (N.S.), Mediterranean (Central) (W.C.), and Agulhas Current (A.G.) sub-datasets, showing predictions at various timestamps. The first row represents the input, the second row shows the ground truth, and the remaining rows display the predictions from different baselines.

els successfully predict the approximate locations of land, sea, and clouds. However, they still face challenges in recovering fine details, often producing blurred predictions. The inherent ambiguity between clouds and fog further exacerbates this issue. Since the distinction between clouds and fog in images primarily relies on texture features, addressing the blurriness in forecasting tasks remains a critical area for further research and practical applications.

6.3. Numerical results for multi-region marine fog forecasting

For the multi-region study on marine fog forecasting, we expanded and combined six independent regional sub-datasets (D.W., D.C., D.E., N.S., Na., and A.G.) into three additional multi-region datasets: Europe (EU), Africa (AF), and an all-mixed-region (All) sub-dataset. This resulted in a total of nine training-testing datasets. In the main text, we provide

Table 3. Numerical results of multi-regional marine fog forecasting using MeteoSat data: The vertical axis represents training data, the horizontal axis represents testing data, and the evaluation metric is MSE.

	D.W	D.C.	D.E.	N.S	Na.	A.G.	EU	AF	All
D.W	3297.54	3282.32	2898.87	3403.72	4473.63	4799.60	3035.57	4525.23	3532.13
D.C.	3625.57	2871.94	2903.75	3678.48	4611.16	4994.77	3106.74	4570.14	3594.55
D.E.	3607.14	3122.68	2694.88	3385.61	4410.14	4843.56	3071.27	4375.08	3505.88
N.S	3720.67	3611.19	3204.69	3086.77	4994.32	5404.97	3129.58	4553.46	3604.21
Na.	6824.00	4528.50	4808.71	6066.23	2829.41	3987.79	4358.33	4171.52	4296.06
A.G.	4877.08	3700.96	3607.50	4305.96	3297.16	3686.85	3558.05	3669.39	3595.16
EU	3080.94	2602.41	2389.33	2789.63	3846.61	4274.99	2613.30	3814.77	3013.79
AF	4627.41	3620.35	3453.36	3985.83	2674.96	3461.31	3412.20	3113.20	3312.53
All	**3028.84**	**2550.35**	**2350.13**	**2675.21**	**2558.98**	**3258.83**	**2525.48**	**2865.53**	**2638.83**

Table 4. Numerical results of multi-regional marine fog forecasting using MeteoSat data: The vertical axis represents training data, the horizontal axis represents testing data, and the evaluation metric is MAE.

	D.W	D.C.	D.E.	N.S	Na.	A.G.	EU	AF	All
D.W.	17992.21	16243.24	15860.19	17327.24	20022.21	20702.67	16787.16	20826.78	18133.71
D.C.	19356.65	14437.33	15639.84	18367.65	19916.18	20670.39	16967.04	20520.45	18151.52
D.E.	19074.67	15418.43	14798.46	17333.34	19426.61	20502.34	16867.83	20063.65	17933.11
N.S.	19515.29	17767.97	17273.84	16541.97	21545.55	22315.07	17293.62	20895.08	18494.11
Na.	27287.62	19259.11	20778.01	24545.69	15084.32	18061.48	20641.25	19513.41	20265.30
A.G.	22878.98	17691.03	18214.64	20641.46	16715.02	17400.91	18608.72	18224.77	18480.75
EU	17043.17	13306.97	13555.79	15188.19	17890.82	18919.63	15158.63	18647.41	16321.57
AF	22166.88	17197.89	17607.70	19594.77	14542.30	16566.12	18138.63	16182.90	17486.72
All	**16876.63**	**13105.42**	**13361.39**	**14879.96**	**13980.45**	**15801.32**	**14558.09**	**15170.83**	**14762.34**

Table 5. Numerical results of multi-regional marine fog forecasting using MeteoSat data: The vertical axis represents training data, the horizontal axis represents testing data, and the evaluation metric is SSIM.

	D.W	D.C.	D.E.	N.S	Na.	A.G.	EU	AF	All
D.W.	0.5533	0.6225	0.6281	0.6211	0.5227	0.4980	0.5988	0.4992	0.5656
D.C.	0.5360	0.6656	0.6357	0.6057	0.5381	0.5185	0.6031	0.5195	0.5753
D.E.	0.5404	0.6459	0.6497	0.6181	0.5497	0.5265	0.6067	0.5280	0.5805
N.S.	0.5267	0.6115	0.6129	0.6279	0.5150	0.4942	0.5912	0.5067	0.5631
Na.	0.4687	0.5820	0.5818	0.5463	0.6273	0.5597	0.5375	0.5279	0.5343
A.G.	0.4949	0.5996	0.5992	0.5745	0.5902	0.5707	0.5746	0.5561	0.5685
EU	0.5811	0.6948	0.6785	0.6592	0.5876	0.5647	0.6325	0.5498	0.6050
AF	0.5094	0.6183	0.6180	0.5889	0.6474	0.6014	0.5875	0.5945	0.5899
All	**0.5866**	**0.7013**	**0.6848**	**0.6658**	**0.6659**	**0.6260**	**0.6527**	**0.6243**	**0.6432**

heatmap visualizations to intuitively illustrate the evaluation results. Here, we supplement these visualizations with the detailed numerical results of the TAU method [9], measured using MSE, MAE, SSIM, and PSNR, as shown in Table 3-Table 6.

6.4. Quantitative results of different positive and negative sample ratios in other regions

Building on the main text, we provide a comparison of model performance under varying positive-to-negative sample ratios (1:1, 2:1, 1:0) on the B.C. and G.A. sub-datasets, evaluated using multiple metrics including Recall, Precision, mAcc, and mIoU, as shown in Table 7 and Table 8, respectively. The results demonstrate that different positive-to-negative ratios lead to variations in performance and generalization across baseline methods. This finding underscores that the proposed MFogHub dataset not only supports multi-region and multi-satellite studies but also enables deeper research into the construction of marine fog datasets. These insights can guide the development of future datasets and advance understanding of the fundamental patterns underlying marine fog monitoring and forecasting tasks.

Table 6. Numerical results of multi-regional marine fog forecasting using MeteoSat data: The vertical axis represents training data, the horizontal axis represents testing data, and the evaluation metric is PSNR.

	D.W	D.C.	D.E.	N.S	Na.	A.G.	EU	AF	All
D.W.	18.15	18.82	18.91	18.10	16.97	16.73	18.65	16.84	18.05
D.C.	17.74	19.66	18.90	17.73	16.89	16.62	18.59	16.89	18.03
D.E.	17.78	19.15	19.27	18.12	17.04	16.70	18.64	17.02	18.10
N.S.	17.63	18.11	18.40	18.50	16.46	16.12	18.45	16.77	17.89
Na.	15.17	17.44	16.91	15.73	18.94	17.54	17.04	17.21	17.10
A.G.	16.52	18.20	17.94	17.00	18.26	17.85	17.91	17.72	17.85
EU	18.52	20.20	19.83	19.03	17.70	17.32	19.40	17.63	18.81
AF	16.77	18.40	18.16	17.41	19.18	18.18	18.16	18.51	18.28
All	**18.60**	**20.31**	**19.91**	**19.23**	**19.39**	**18.47**	**19.63**	**18.93**	**19.40**

References

[1] Radhakrishna Achanta, Appu Shaji, Kevin Smith, Aurelien Lucchi, Pascal Fua, and Sabine Süsstrunk. Slic superpixels compared to state-of-the-art superpixel methods. *IEEE transactions on pattern analysis and machine intelligence*, 34(11):2274–2282, 2012. 2

[2] Huang Bin, Wu Ming, Zhu Shuyue, Zhao Wei, Cui Zhanbei, and LYU Cheng. Sea fog monitoring method based on deep learning satellite multi-channel image fusion (in chinese). *Meteorological Science and Technology*, 49(6):823–829, 2021. 1

[3] Liang-Chieh Chen, Yukun Zhu, George Papandreou, Florian Schroff, and Hartwig Adam. Encoder-decoder with atrous separable convolution for semantic image segmentation. In *Proceedings of the European conference on computer vision (ECCV)*, pages 801–818, 2018. 8

[4] Alexey Dosovitskiy, Lucas Beyer, Alexander Kolesnikov, Dirk Weissenborn, Xiaohua Zhai, Thomas Unterthiner, Mostafa Dehghani, Matthias Minderer, Georg Heigold, Sylvain Gelly, et al. An image is worth 16x16 words: Transformers for image recognition at scale. *arXiv preprint arXiv:2010.11929*, 2020. 8

[5] Ali Hatamizadeh, Ziyue Xu, Dong Yang, Wenqi Li, Holger Roth, and Daguang Xu. Unetformer: A unified vision transformer model and pre-training framework for 3d medical image segmentation. *arXiv preprint arXiv:2204.00631*, 2022. 8

[6] Rui Li, Shunyi Zheng, Ce Zhang, Chenxi Duan, Libo Wang, and Peter M Atkinson. Abcnet: Attentive bilateral contextual network for efficient semantic segmentation of fine-resolution remotely sensed imagery. *ISPRS Journal of Photogrammetry and Remote Sensing*, 181:84–98, 2021. 8

[7] Research Data Archive, Computational and Information Systems Laboratory, National Center for Atmospheric Research,

Table 7. Quantitative results of five evaluation metrics for eight baseline methods under different positive-to-negative sample ratios on the GOES16 satellite Baja California (B.C.) region sub-dataset.

	B.C. sub-dataset (pos:neg=198:192)					**B.C. sub-dataset (pos:neg=198:81)**					**B.C. sub-dataset (pos:neg=198:0)**				
	CSI	**Rec**	**Pre**	**mIoU**	**mAcc**	**CSI**	**Rec**	**Pre**	**mIoU**	**mAcc**	**CSI**	**Rec**	**Pre**	**mIoU**	**mAcc**
Deeplabv3p [3]	17.71	18.59	78.86	56.85	59.18	20.73	22.39	73.62	58.37	61.00	25.53	32.26	55.01	60.56	65.49
UNet [8]	25.06	30.71	57.65	60.38	64.81	31.30	40.15	58.68	63.58	69.39	40.48	**73.06**	47.58	67.68	**84.59**
Unetpp [13]	**42.25**	**59.39**	59.40	**69.20**	**78.72**	43.58	**72.20**	52.36	69.56	**84.52**	38.99	66.30	48.63	67.03	81.46
ABCNet [6]	16.81	21.22	54.02	55.96	59.98	21.68	24.22	67.36	58.80	61.83	38.96	52.93	59.60	67.52	75.60
BANet [11]	28.10	56.57	35.83	60.63	75.84	37.74	40.67	83.97	67.30	70.15	**47.66**	63.75	**65.38**	**72.17**	81.06
Unetformer [5]	39.86	56.06	57.97	67.93	77.05	42.54	56.05	63.84	69.48	77.26	43.81	69.72	54.11	69.78	83.43
ViT [4]	23.99	24.18	**96.85**	60.21	62.07	**43.97**	47.36	86.03	**70.57**	73.49	39.01	56.63	55.63	67.41	77.22
DlinkViT [12]	6.66	6.68	96.73	51.17	53.33	40.36	41.35	**94.39**	68.75	70.62	38.63	59.35	52.53	67.08	78.38

Table 8. Quantitative results of five evaluation metrics for eight baseline methods under different positive-to-negative sample ratios on the GOES16 satellite Gulf of Alaska (G.A.) region sub-dataset.

	G.A. sub-dataset (pos:neg=179:157)					**G.A. sub-dataset (pos:neg=179:85)**					**G.A. sub-dataset (pos:neg=179:0)**				
	CSI	**Rec**	**Pre**	**mIoU**	**mAcc**	**CSI**	**Rec**	**Pre**	**mIoU**	**mAcc**	**CSI**	**Rec**	**Pre**	**mIoU**	**mAcc**
Deeplabv3p [3]	22.90	28.83	52.70	59.54	63.89	27.40	46.66	39.89	61.25	71.91	14.78	20.11	35.82	55.12	59.32
UNet [8]	23.31	33.29	43.74	59.50	65.78	27.01	43.60	41.53	61.18	70.56	22.70	**41.26**	33.54	58.57	**68.97**
Unetpp [13]	**24.52**	**38.41**	40.41	**59.92**	**68.06**	23.79	**47.71**	32.18	58.86	**71.82**	21.83	42.74	30.86	57.89	69.43
ABCNet [6]	12.17	15.40	36.75	53.91	57.16	32.53	37.46	**71.21**	64.73	68.42	20.71	33.21	35.49	57.85	65.38
BANet [11]	**34.80**	43.23	64.08	**65.80**	71.12	**43.22**	**72.89**	51.50	**69.69**	**85.05**	**33.27**	48.33	**51.64**	**64.71**	73.25
Unetformer [5]	32.87	**51.95**	47.24	64.33	**74.80**	34.16	51.96	49.93	65.09	74.93	22.99	38.07	36.72	58.98	67.71
ViT [4]	21.48	26.03	**55.12**	58.87	62.59	**36.64**	44.90	66.57	**66.78**	71.99	27.18	38.07	48.73	61.58	68.23
DlinkViT [12]	32.32	38.48	**66.86**	64.57	68.86	42.05	54.28	**65.11**	69.54	76.55	**33.62**	**52.93**	47.96	**64.74**	**75.30**

University Corporation for Atmospheric Research, Physical Sciences Laboratory, Earth System Research Laboratory, OAR, NOAA, U.S. Department of Commerce, Cooperative Institute for Research in Environmental Sciences, University of Colorado, National Oceanography Centre, University of Southampton, Met Office, Ministry of Defence, United Kingdom, Deutscher Wetterdienst (German Meteorological Service), Germany, Department of Atmospheric Science, University of Washington, Center for Ocean-Atmospheric Prediction Studies, Florida State University, and National Centers for Environmental Information, NESDIS, NOAA, U.S. Department of Commerce. International comprehensive ocean-atmosphere data set (icoads) release 3, individual observations, 2016. 1

[8] Olaf Ronneberger, Philipp Fischer, and Thomas Brox. U-net: Convolutional networks for biomedical image segmentation. In *Medical Image Computing and Computer-Assisted Intervention–MICCAI 2015: 18th International Conference, Munich, Germany, October 5-9, 2015, Proceedings, Part III 18*, pages 234–241. Springer, 2015. 8

[9] Cheng Tan, Zhangyang Gao, Lirong Wu, Yongjie Xu, Jun Xia, Siyuan Li, and Stan Z Li. Temporal attention unit: Towards efficient spatiotemporal predictive learning. In *Proceedings of the IEEE/CVF Conference on Computer Vision and Pattern Recognition*, pages 18770–18782, 2023. 7

[10] Haiping Wang, Zenghai Zhang, Yiwu Huang, and Lin Dong. Spring 2024 marine weather review (in chinese). *Journal of Marine Meteorology*, 44(3):162–172, 2024. 1, 2

[11] Libo Wang, Rui Li, Dongzhi Wang, Chenxi Duan, Teng Wang, and Xiaoliang Meng. Transformer meets convolution: A bilateral awareness network for semantic segmentation of very fine resolution urban scene images. *Remote Sensing*, 13 (16):3065, 2021. 8

[12] Haotian Yan, Sundingkai Su, Ming Wu, Mengqiu Xu, Yihao Zuo, Chuang Zhang, and Bin Huang. Seamae: Masked pre-training with meteorological satellite imagery for sea fog detection. *Remote Sensing*, 15(16):4102, 2023. 4, 5, 8

[13] Zongwei Zhou, Md Mahfuzur Rahman Siddiquee, Nima Tajbakhsh, and Jianming Liang. Unet++: Redesigning skip connections to exploit multiscale features in image segmentation. *IEEE transactions on medical imaging*, 39(6):1856–1867, 2019. 8